ELECTROCHEMISTRY

Ultrahigh-rate and ultralong-life aqueous batteries enabled by special pair-dancing proton transfer

Lulu Wang, Jie Yan, Yuexian Hong, Zhihao Yu, Jitao Chen*, Junrong Zheng*

The design of Faradaic battery electrodes with high rate capability and long cycle life comparable to those of supercapacitors is a grand challenge. Here, we bridge this performance gap by taking advantage of a unique ultrafast proton conduction mechanism in vanadium oxide electrode, developing an aqueous battery with untrahigh rate capability up to 1000 C (400 A g^{-1}) and extremely long life of 0.2 million cycles. The mechanism is elucidated by comprehensive experimental and theoretical results. Instead of slow individual Zn^{2+} transfer or Grotthuss chain transfer of confined H^+, the ultrafast kinetics and excellent cyclic stability are enabled by rapid 3D proton transfer in vanadium oxide via the special pair dance switching between Eigen and Zundel configurations with little constraint and low energy barriers. This work provides insight into developing high-power and long-life electrochemical energy storage devices with nonmetal ion transfer through special pair dance topochemistry dictated by hydrogen bond.

INTRODUCTION

Batteries offer high energy density but lack high power density and long cycle life of supercapacitors (*1*). There is a growing demand for rapid energy storage (high power) without compromising energy density. However, increasing the power density and cycle life of battery electrodes remains a grand challenge (*2*, *3*). The charge storage mechanisms of Faradaic electrodes dictate their rate capability to be dependent on the choice of ion charge carriers (*2*, *4*). State-of-the-art electrochemical energy storage devices are focused on metal ions (e.g., Li^+, Na^+, and Mg^{2+}) shuttling charges (*5*–*8*), where the ion-electrode interaction is purely ionic and very strong, and the metal ions must individually diffuse distances much longer than their sizes, leading to sluggish kinetics. On the other hand, the smallest nonmetal cation, H^+, of which the mobility in water is at least 4.5 times larger than any other cations, can notably facilitate the charge/discharge rate of metal-organic frameworks (*9*, *10*) and organic compound electrodes (*11*, *12*). However, proton batteries require corrosive acidic electrolytes, and their cycle life drops more than two orders of magnitudes in full batteries when combined with solid-state anodes (*10*, *13*). In mild electrolytes, proton (de)insertion [with or without metal cation co-(de)insertion] can also occur in inorganic cathodes, e.g., MnO_2, MoO_3, and V_xO_y, but the power densities and cycle stability of these batteries are limited by unidirectional confined proton transfer mechanism (*14*–*20*), e.g., the Grotthuss chain–like transfer, which are far from the practical demands (10 kW kg^{-1} versus 100 kW kg^{-1}, 1000 cycles versus 10,000 cycles). It remains unanswered why the proton transfer is confined and much slower than expected inside these inorganic electrodes, and whether it is feasible to fully use the intrinsic mobility of proton to increase the power density and cycle stability of batteries to be comparable to those of supercapacitors.

More than 200 years ago, Grotthuss suggested a chain mechanism for shuttling hydrogen atoms (*21*). As displayed in Fig. 1A, the mechanism was revived as for proton mobility when ions and protons were discovered, where a proton bridging two water molecules switches its partner from one molecule to the other, kicking away one hydrogen from its adopted molecule and triggering a chain of similar displacements (*22*, *23*). Recent theoretical studies (*24*–*27*), however, suggest that the molecular mechanism of proton transfer is far beyond the simplified chain transfer. As displayed in Fig. 1 (B and C), it is a hierarchical process of multiple steps and multiple time scales, involving partner exchange, selection, rattling, and settling into a new Eigen configuration. The activation enthalpy for proton transfer is concealed in the selection step that allows the distorted Zundel intermediate to form. The special pair dance mechanism randomizes the proton hopping direction, which renders a three-dimensional (3D) diffusive proton transfer behavior, thus reducing constraints on proton transfer and lowering the energy barrier. Accordingly, maintaining this unique transfer mechanism is crucial for proton to retain its intrinsic mobility in cathode as to improve the electrochemical kinetics of the faradaic battery electrodes.

In many inorganic cathode materials, the spacing in the lattice is too small to contain sufficient water molecules to solvate proton, which greatly limits the proton-water partner exchange and selection processes. Therefore, the unique special pair dance mechanism hardly works in these electrode materials. In addition, the dynamics of the solvent water molecules, according to ultrafast infrared measurements and theory (*28*–*30*), are notably slowed down in such a small confined volume. Both insufficient solvation and slow dynamics of confined water molecules would lead to sluggish proton transfer kinetics in the cathodes where proton (de)insertions were reported to play roles (*31*, *32*).

In light of the importance of solvation structure and dynamics of proton for its transfer kinetics, we design a layered hydrated vanadium oxide cathode material containing abundant lattice water to allow a hierarchical and multidirectional concerted cleavage and formation of hydrogen bond (HB) to rapidly shuttle H^+ via the special pair dance mechanism. Although there are no precedent examples that such a unique mechanism could occur in vanadium oxide cathode, molecular dynamic simulations and nudged elastic band calculations strongly suggest its occurrence in our vanadium

College of Chemistry and Molecular Engineering, Beijing National Laboratory for Molecular Sciences, Peking University, Beijing 100871, China.
*Corresponding author. Email: junrong@pku.edu.cn (J.Z.); chenjitao@pku.edu.cn (J.C.)

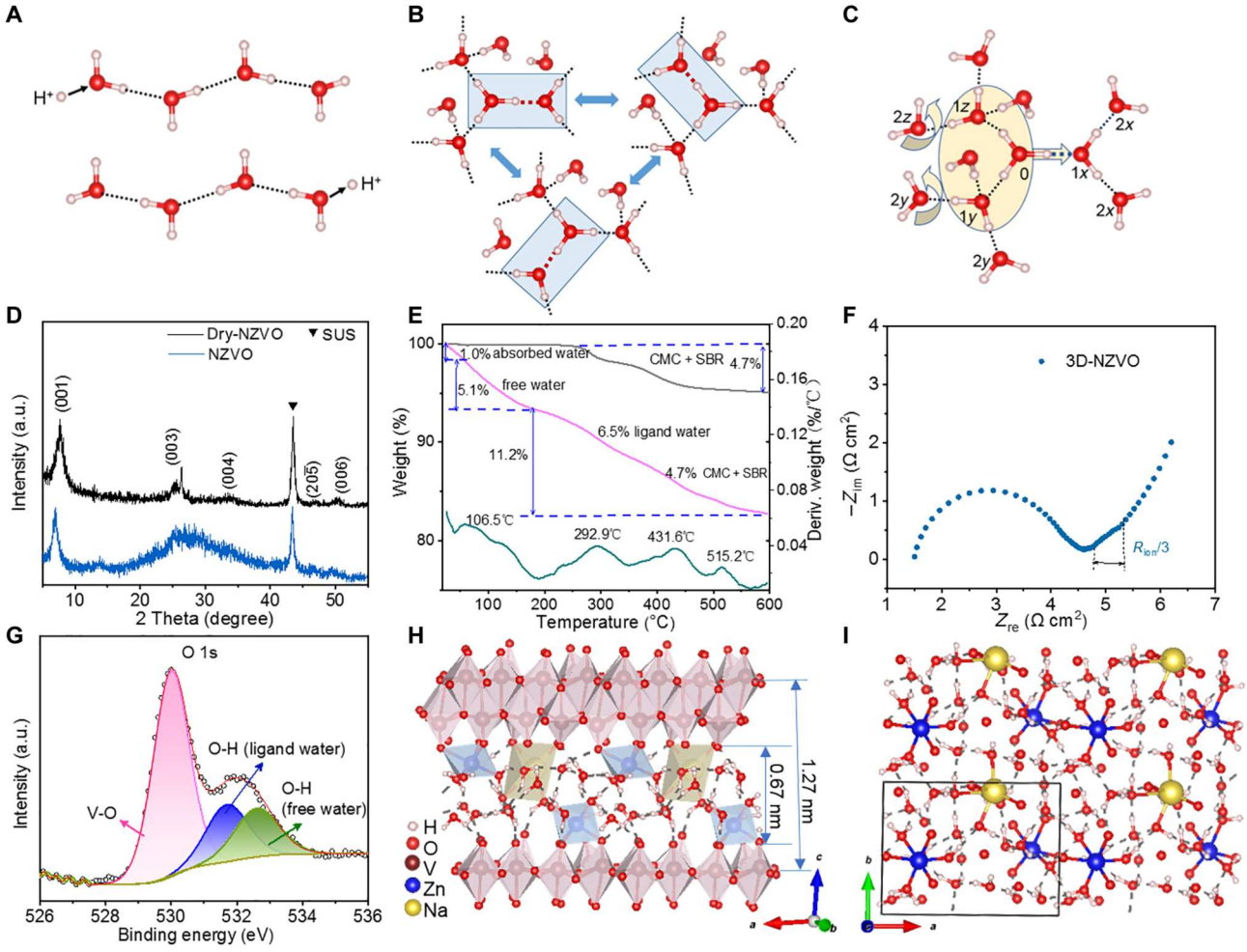

Fig. 1. Structural characterizations of NZVO. (**A**) Schematic representation of the Grotthuss chain transport mechanism, in which proton conduction is operated by rearranging HBs along a water chain (oxygens in red and hydrogens in white). (**B**) Schematic depiction of the "special pair dance" occurring in the first solvation shell of hydronium in its "resting state" (during the long trajectory segments of no-proton transfer). (**C**) Schematic depiction of the "selection phase" leading into the transitional Zundel structure ($H_5O_2^+$) of the proton mobility mechanism. (**D**) XRD patterns of NZVO electrode and wet NZVO electrode immersed in an aqueous electrolyte. (**E**) TGA and derivative thermogravimetry (DTG) curves of 70% NZVO/24% conductive carbon/6% CMC + SBR mixture under nitrogen atmosphere at a heat ramp of 10°C/min. (**F**) Nyquist plots obtained from potentiostatic EIS of a symmetric cell using two identical NZVO electrodes at a state of charge (SOC) 0%. (**G**) High-resolution O 1s region of the XPS spectra of NZVO electrode. (**H**) Calculated water orientations in a 2 × 1 × 1 supercell of NZVO. (**I**) Orientations and connections of hydrogen-bonded water molecules in 2 × 2 × 1 supercell of NZVO, where the framework is omitted for clarity.

oxide material, which remarkably improves the charge transfer kinetics and consequently tunes the ratio of H^+/Zn^{2+} as charge shuttles dependent on the charge/discharge rate. As a result, the battery with this vanadium oxide cathode owns both high energy density of metal ion batteries and high power density and long cycle life of supercapacitors, and reaches a combination of an ultralong cycle life and a high power density: a cycle life of 0.2 million cycles at 500 C (200 A g^{-1}, 80 mA cm^{-2}) with a power density of 162 kW kg^{-1} at an energy density of 103.6 Wh kg^{-1} (based on the mass of cathode active material only).

RESULTS

Characterization of 3D NZVO network cathode

NZVO ($Na_{0.12}Zn_{0.25}V_2O_5{\cdot}2.5H_2O$) was obtained by in situ electrochemical activation (fig. S1) of electrodeposited NVO ($Na_{0.27}V_2O_5{\cdot}1.53H_2O$) (fig. S2) in coin cells using a Zn foil anode, a 3 M $Zn(CF_3SO_3)_2$ electrolyte, and a glass fiber separator. In detail, the cell is galvanostatically cycled at a low rate of 0.2 A g^{-1}, and the specific capacity increases continuously, reaching 436 mA·hour g^{-1} after three cycles (fig. S1A). The initial cyclic voltammetry (CV) curve of the battery slightly differs from the subsequent ones, indicating the gradual electrochemical activation of NVO. The inductively coupled plasma–optical emission spectroscopy (ICP-OES) analysis of the electrodes shows that several preintercalated sodium ions were replaced by zinc ions after three cycles. The (001) peak of NVO at 8.02° (fig. S3A) shifts to 6.94° (Fig. 1D) after three cycles, indicating that the corresponding (001) interlayer space increases from 11.0 Å (fig. S3B) to 12.7 Å. The (001) peak of NZVO shifts from 6.94° to 7.74° upon drying at room temperature, and the (001) interlayer space decreases to 11.4 Å (fig. S4) due to the

loss of partial interlayer free water, leading to the formation of dry-NZVO. Moreover, the loss and gain of partial interlayer free water of NZVO at room temperature are reversible. The stoichiometric formula of NVO and dry-NZVO is determined to be $Na_{0.27}V_2O_5{\cdot}1.53H_2O$ and $Na_{0.12}Zn_{0.25}V_2O_5{\cdot}2.2H_2O$ by combining ICP-OES (table S1) and thermogravimetric analysis (TGA) studies (Fig. 1E and fig. S5). Specifically, ~1.0% weight loss up to 42°C can be attributed to the absorbed water (Fig. 1E). Additional weight loss of 5.1% appears from 42° to 190°C, primarily due to the loss of interlayer free water. The weight loss of 11.2% corresponds to the loss of interlayer ligand water (~6.5%) (~292.9°C) and decomposition of the carboxymethylcellulose (CMC)/styrene-butadiene rubber (SBR) (~4.7%). On the basis of the above analysis, there are ~7 free water molecules and ~10 ligand water molecules in each unit cell of dry-NZVO ($1Na2Zn16V40O{\cdot}17H_2O$). The hydration degree of the NZVO electrode can be controlled by keeping the same electrodeposition condition of NVO and charge/discharge current density during electrochemical activation condition of NVO, thus assuring consistent performance.

The scanning electron microscopy (SEM) image of NZVO (fig. S6) displays a 3D network morphology composed of interconnected nanobelts with high porosity. Transmission electron microscopy (TEM) images (fig. S7) also confirm the interconnected network architecture, in which NZVO nanobelts have a width about 35 nm. The N_2 adsorption/desorption isotherm of NZVO (fig. S8) presents a typical type intravenous curve with an H3 hysteresis, suggesting the formation of mesoporous structure. The Brunauer-Emmett-Teller–specific surface area reaches 91.6 $m^2\ g^{-1}$, which is much larger than previously reported cathodes of zinc-ion batteries (ZIBs) (*14*, *33*). Moreover, the compaction density of NZVO increases with the pressure, reaching ~2.62 g cm^{-3} under the pressure of 200 MPa (fig. S9). To reveal the effect of structural features on the charge transport kinetics, we used electrochemical impedance spectroscopy (EIS) measurements of two identical electrodes in a symmetric cell configuration. As shown in Fig. 1F, Nyquist plot of two electrodes exhibits similar 45° slopes in the frequency region between ~1 and 100 Hz and quasi-vertical lines at low frequency (<1 Hz), indicating a nonfaradaic process in porous electrodes validated by the transmission line model (TLM) (*34*, *35*). The projection of the 45° slope to the real axis is defined as $R_{ion}/3$, reflecting the ionic resistance inside a porous electrode and the rate capability of a porous electrode (*35*). The low ionic resistance (R_{ion}) value (1.8 ohm cm^2) of 3D porous NZVO electrodes suggests that the ion transport kinetics can be improved by introducing pores in the electrode (*36*). The large pores serve as ion transport shortcuts in the hierarchical structure and greatly improve ion access to the NZVO surface, facilitating rapid ion transport throughout the entire electrode. In addition, the porous NZVO offers abundant contact interfaces with conductive agents, reducing the electronic resistance. In short, the porous morphology produces interpenetrating both electron and ion transport paths, favoring fast electrochemical kinetics. As shown in Fig. 1G, the O 1s x-ray photoelectron spectroscopy (XPS) region of NZVO is deconvoluted to three components at 530.1, 531.6, and 532.6 eV. The peaks at 530.1 eV can be attributed to VOx, whereas the high-energy O 1s peaks at 531.6 and 532.6 eV correspond to the ligand water and free water (*37*), respectively, consistent with the TGA result.

To further obtain the NZVO crystalline structure with the HB network mediating proton conduction, density functional theory (DFT) calculations were performed on the basis of structural characterization including x-ray diffraction (XRD), TGA, and XPS results. The characteristic diffraction peaks of NZVO can be well indexed to a layered $Zn_{0.25}V_2O_5{\cdot}nH_2O$ phase, where a double-sheet type 2D V_2O_5 layers are pinned by indigenous Zn^{2+} and lattice water stack along the *c* axis and extend infinitely in the *a*-*b* plane. There are ~10 ligand water molecules in each unit cell of NZVO, but the amount of free water cannot be obtained by TGA analysis. Thus, we optimized the wet NZVO structure by DFT calculations to determine the amount of interlayer free water based on the interlayer distance. Calculations were carried out using a $2 \times 1 \times 1$ supercell. The interlayer distance of NZVO gradually increases with the amount of interlayer free water, reaching ~1.27 nm with 10 free water molecules. As shown in Fig. 1H, the optimal amount of interlayer water molecules is 20 (10 free water and 10 ligand water molecules) in each unit cell of wet NZVO ($1Na2Zn16V40O{\cdot}20H_2O$), in which water molecules randomly distribute. DFT calculations were further conducted to screen the energetically favorable configuration for collections of water molecules confined in the V_2O_5 layers. After relaxation, the free water and ligand water jointly constitute an HB network (Fig. 1I). Since Na^+ and Zn^{2+} have different crystallographic positions, various models of NZVO with different arrangements of Na^+ and Zn^{2+} are considered (fig. S10). The model with the lowest total energy (Fig. 1H) corresponds to the most stable structure of NZVO. The calculated results demonstrate a typical layered structure assigned to the triclinic system (table S2). The interlayer free water, ligand water (about two layers of water), and two layers of terminal O coordinated with V cooperatively constitute a 3D interconnected and dense HB network in the interlayer of NZVO, which is ~0.67 nm in height (along the *c* axis) and extends infinitely in the 2D *a*-*b* plane (Fig. 1I). The 3D contiguous and populous HB network offers indispensable solvation environment for proton, which allows a hierarchical and multidirectional concerted cleavage and formation of HB to rapidly shuttle H^+ via the special pair dance mechanism switching between Eigen and Zundel configurations with little constraint and low energy barriers. The ligand water strongly bound to Zn^{2+} or Na^+ acts in concert with Zn^{2+} or Na^+ to serve as pillars of the host framework, which plays a crucial role in stabilizing the HB network and avoiding structural stress and failure, hence ensuring the long-term cycle stability. The free water with high freedom can rapidly make orientation adjustments to reconstruct HB network orientations and configurations for fast proton conduction.

Proton conduction for fast electrochemical kinetics

Scanning TEM (STEM)–energy-dispersive spectroscopy (EDS) (figs. S11 and S12), ex situ XRD (fig. S13), ICP-OES (table S3), and XPS (fig.S14) analyses of NZVO electrode at selected states verified the reversible Zn^{2+}/H^+ (de)intercalation. Moreover, STEM-EDS and ICP-OES analyses of fully discharged NZVO electrode at various rates (fig. S12 and table S3) and the electron transfer number during redox reaction reveal that H^+ insertion becomes more predominant with the increasing charge/discharge rate, almost reaching 100% at 200 A g^{-1} (Fig. 2A). The wider gap in contribution to capacity between H^+ and Zn^{2+} at a higher rate results from their distinctly different transport manners where H^+ is much more mobile.

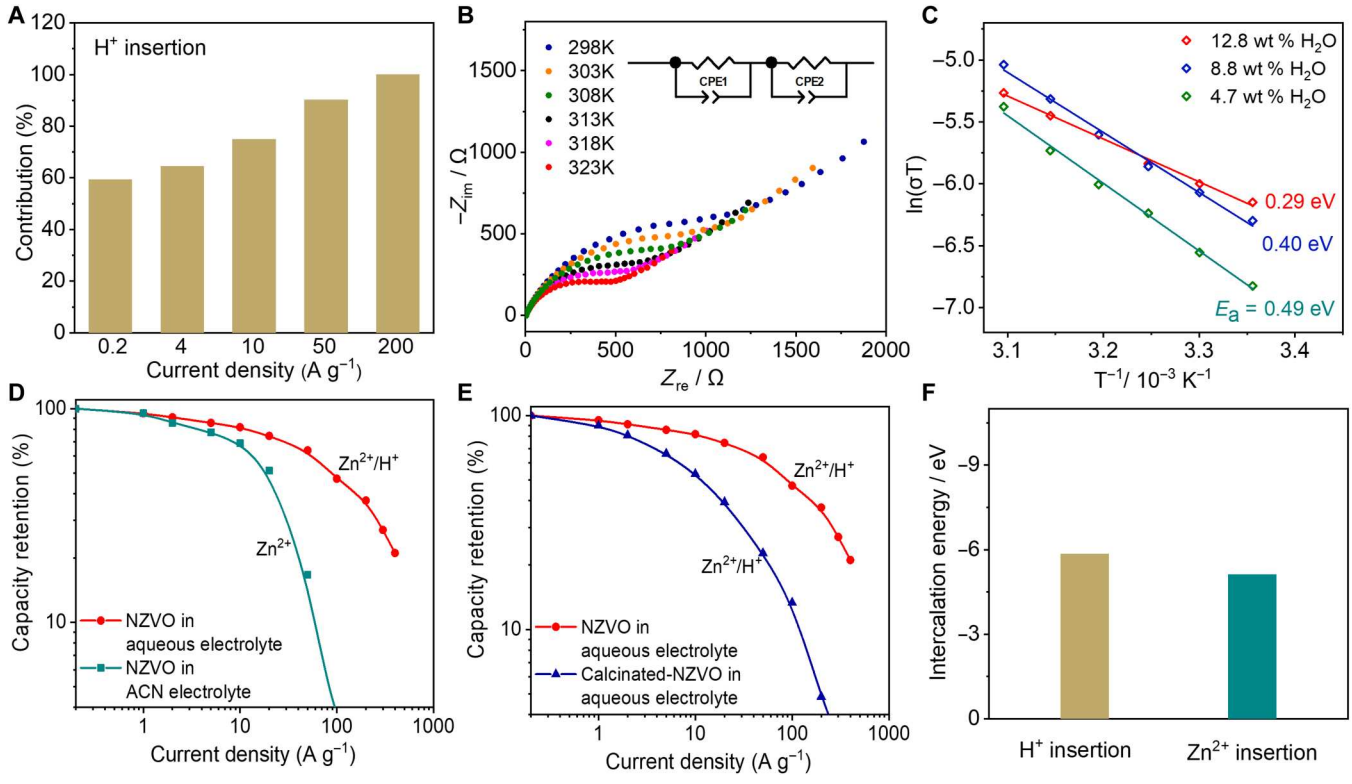

Fig. 2. Proton conduction for fast electrochemical kinetics. (**A**) Capacity contribution of H^+ and Zn^{2+} insertion as a function of charge/discharge rate. (**B**) EIS analyses of NVO at various temperatures and 100% humidity. Inset is the equivalent circuit. R_{bulk} and R_{grain} represent the resistance of the bulk powder and their grain boundaries, respectively. The larger grain boundary resistance may result from the nanosized particles of NVO. (**C**) Plot of ln(σT) versus 1000/T for NVO with various water content. (**D**) Rate performance comparison of NZVO electrode in 3 M $Zn(CF_3SO_3)_2$ aqueous and ACN electrolytes. (**E**) Rate performance comparison between NZVO and calcinated-NZVO electrode in 3 M $Zn(CF_3SO_3)_2$ aqueous electrolyte. (**F**) Comparison of Zn^{2+} and H^+ intercalation energy for NZVO electrode.

To understand the underlying mechanism for this fast H^+ transport kinetics, the proton conductivity of the NVO powder was measured as a function of temperature. As shown in Fig. 2B, the proton conductivity of NVO is 4.0×10^{-6} S cm^{-1} at 298 K and 100% humidity and increases at a higher temperature. By plotting ln (σT) versus 1/T, the activation energy (E_a) for the proton transport through NVO was calculated to be 0.29 eV (Fig. 2C), suggesting a fast proton conduction (E_a < 0.4 eV) (*38*, *39*). Furthermore, the E_a value increases as the interlayer water content decreases (Fig. 2C and figs. S15 and S16), indicating that interlayer water of the NVO electrode is the vital medium for H^+ transport.

To evaluate the role of proton conduction mechanism in facilitating electrochemical kinetics of Zn/NZVO battery, the rate capability of the battery was tested under two different conditions where the proton transfer topochemistry is inviable. The proton conduction is unavailable to the electrode when only Zn^{2+} acts as charge carrier in acetonitrile (ACN) electrolyte, and the battery exhibits a much worse rate performance compared with the aqueous electrolyte (Fig. 2D and fig. S17). Moreover, the V 2p signal of XPS spectra in 3 M $Zn(CF_3SO_3)_2$ ACN electrolyte (fig. S18) shows that fewer V components are reduced with only Zn^{2+} insertion compared to that in 3 M $Zn(CF_3SO_3)_2$ aqueous electrolyte. Another approach to eliminate proton conduction is to interrupt the HB network and remove the contiguous medium for proton displacement inside the electrode by removing the interlayer water of the NVO electrode. The calcinated-NVO [4.7 weight % (wt %) H_2O] owns similar crystal structure as NVO (12.8 wt % H_2O) but much fewer ligand water molecules (fig. S15). As expected, the calcinated-NVO exhibits inferior rate capability and (de)insertion kinetics than the NVO electrode in the same aqueous electrolyte (Fig. 2E and fig. S19). The above control studies demonstrate the fact that abundant lattice water in the electrode and aqueous electrolyte is the indispensable prerequisite for proton conduction, and the proton conduction notably promotes the rate performance of the battery, thus highlighting the correlation between the special fast proton transfer mechanism and high rate capability of proton storage in NZVO. The Zn^{2+} and H^+ intercalation energy for NZVO electrode was also compared in terms of thermodynamics. The calculated H^+ intercalation energy (−5.85 eV) is lower than that of Zn^{2+} intercalation (−5.12 eV), confirming the thermodynamically preferable H^+ intercalation into NZVO (Fig. 2F). In addition to different charge transport manners, the nature of the guest-host interaction is different. Inserted Zn^{2+} interacts directly with the V_2O_5 host. In contrast, there is strong HB between the H^+ ions and the V_2O_5 host and interlayer water, which would lower the Gibbs free energy of the total ion-electrode system.

Proton transfer via special pair dance mechanism in NZVO

The comprehensive experimental results strongly suggest a special fast proton transfer mechanism other than the Grotthuss chain transfer in this system. To probe the proton transfer mechanism and dynamics in the (001) interlayer of NZVO in detail, the first-

principles molecular dynamics (FPMD) simulations were performed in canonical ensemble (NVT) at 300 K for about 16 ps. Since ~10 protons can be stored in each wet NZVO unit cell ($1Na2Zn16V40O{\cdot}20H_2O$) at 200 A g^{-1}, three protons were randomly inserted into the (001) interlayer of each NZVO unit cell to simulate an early stage of the discharge process. By monitoring the FPMD trajectories, we found VO-water and in-water proton transfer events in (001) interlayers during the simulation time scale. The typical snapshots of this proton transfer are shown in fig. S20. The frequency of in-water proton transfer (86%) is much higher than the VO-water proton transfer (14%) by counting the proton transfer events occurring along the trajectory (Fig. 3A).

To investigate how proton transfer in (001) interlayer water is different from that in bulk water, the behavior of hydronium in the periods between proton transfer events was characterized. We define the O atom in the hydronium as O_0, the closet O atom in the first solvation shell as O_{1x}, and the other two as O_{1y} and O_{1z} according to their increasing distance from the hydronium (Fig. 3B) (*25*). We can monitor the variation in identity of O_0, O_{1x}, O_{1y}, and O_{1z} as a function of time. Figure 3C and fig. S21A displays how the identity of O_0 and O_{1x} varies during a typical trajectory segment of 0.3 ps. During these "short" segments, the fluctuations between the same two values reflect the rapid O_0 and O_{1x} identity interchange, resulting from the proton rapid movement between O_0 and O_{1x}. In this case, the O_0-H and O_{1x}-H bond lengths are close (Fig. 3D and fig. S21B). During the "long" segments, O_0 maintains its value, while O_{1x} fluctuates among three values, that is, the three water ligands in the first solvation shell of the hydronium. The O_0-H bond is much shorter than the O_{1x}-H bond. From the above discussion, it is speculated that the

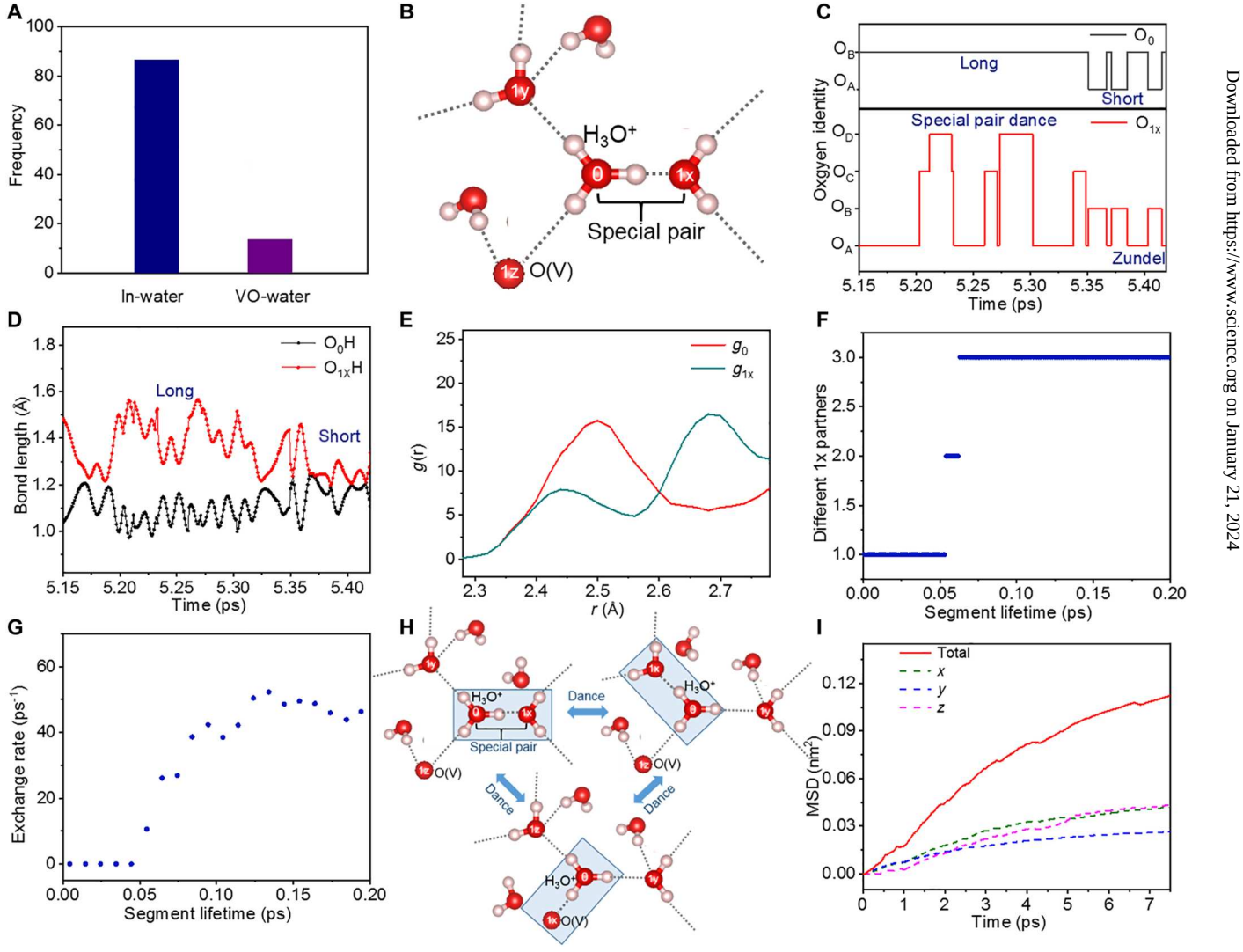

Fig. 3. FPMD simulations of proton transfer in NZVO. (**A**) Frequency of VO-water and in-water proton transfer events. (**B**) Typical solvation structure of hydronium, H_3O^+, in hydrated NZVO. (**C**) Time dependence of the identity of the hydronium oxygen atom, O_0, and its nearest neighbor oxygen, O_{1x}. (O_A, O_B, O_C, and O_D represent different water or VO oxygen atoms.) (**D**) O-H bond lengths from trajectory segments during a typical proton transfer event. (**E**) Two RDFs as calculated from the complete time sequence of several simulation algorithms. (**F**) Average number of different special partners, O_{1x}, as a function of the nontransfer interval length. (**G**) Average rate of exchanging the 1*x* partner. (**H**) Schematic depiction of the "special pair dance" occurring in NZVO. (**I**) Total and decomposed MSD of the O_0 atom.

hydronium has the transition structure of "the Zundel cation" [$H_5O_2^+$ or $H_3O^+O(V)$], whereby the O_0 and O_{1x} atoms share the proton during the short segments, whereas the "long" segments correspond to the distorted Eigen state of the hydronium {H_3O^+[3H_2O] or H_3O^+[2H_2O1O(V)]}, whereby the identity of O_0 remains constant and the identity of special partner (O_{1x}) interchanges rapidly among the three first-shell water ligands via special pair dance of three O_1 atoms (*40*). The radial distribution function (RDF), $g(r)$, centered on the first-shell oxygen atoms was calculated to validate whether the structure of the solvated proton is a distorted Eigen cation. As shown in Fig. 3E, $g_0(r)$ (the RDF for the hydronium) and $g_{1x}(r)$ (the RDF for nearest neighbor) exhibit obviously distinct solvation structures. $g_0(r)$ owns a single broad peak, while $g_{1x}(r)$ has one peak at 2.44 Å due to the HB with O_0 and another peak at 2.68 Å arising from HBs with O_{2x} in the second shell. Thereby, the hydronium structure in the (001) interlayer is an asymmetric Eigen cation centered on O_0 that forms short HB with O_{1x} via special pair.

Moreover, the distorted Eigen cation is not static. Instead, the identity of O_{1x} constantly changes. To verify the partner switch statistically, we examine the average number of different 1*x* partners as a function of time where the most hydronium-like oxygen does not change. There is only one special partner (O_{1x}) and a zero exchange rate for short segments (Fig. 3, F and G), which are thus dominated by the tight Zundel complexes. With the increasing time in which the proton resides on a single water molecule, the number of partners increases to three and the exchange rate increases to about one per 50 fs, indicative of an Eigen complex where the special partner switches dynamically.

In summary, the proton transfer in NZVO follows the Eigen-Zundel-Eigen mechanism as in the bulk water via the special pair dance (Fig. 3H and movie S1). The special pair dance rapidly randomizes the proton hopping direction, making the proton transfer of interlayer-confined water a random walk-diffusive process, rather than a coherent transfer over a chain of water molecules as Grotthuss proposed.

Since the key for proton transfer is the variation of the O_0 identity (Fig. 3H), we calculated the mean square displacement (MSD) of the O_0 atoms and further decomposed MSD in the *x*, *y*, and *z* axis to further track the proton motion in the interlayer. In the case of interlayer water and bulk water (Fig. 3I), MSDs both distribute uniformly in the three directions. In other words, the proton transfer is 3D-like. The simulated diffusion coefficients (D) from MSD for protons in the (001) interlayer is 2.5×10^{-9} m^2 s^{-1} (fig. S22), at the same order of the experimental value (9.31×10^{-9} m^2 s^{-1}) in bulk water (*40*).

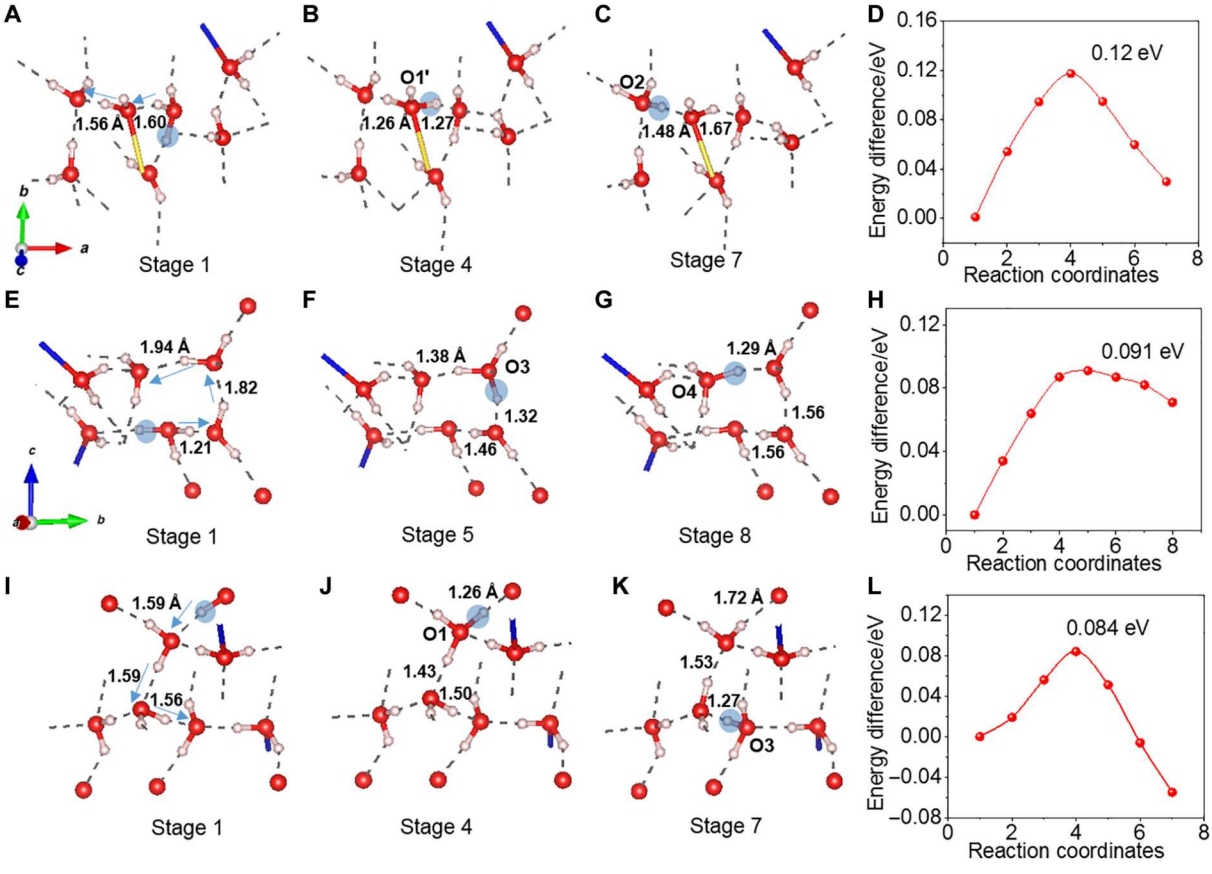

Fig. 4. DFT calculations of proton migration pathway. (**A** to **C**) Configurations of the protonated NZVO structure at different selected transition stages and (**D**) the relative energy of different transition stages during the proton transport process from free water to the neighboring ligand water and then to the next free water. (**E** to **G**) Configurations of the protonated NZVO structure at different selected transition stages and (**H**) the relative energy of different transition stages during the proton transport process among free waters. (**I** to **K**) Configurations of the protonated NZVO structure at different selected transition stages and (**L**) the relative energy of different transition stages during the proton transport process from VO to free waters (the blue arrows in stage 1 represent the proton migration pathway).

Proton transfer path and corresponding energy barrier

The energy barriers of the proton transfer were further calculated. We first determine the energetically favorable H^+ binding site by DFT calculations. The inserted H^+ in NZVO can bind with interlayer water to form hydronium-H_3O^+ and other forms (*21*, *41*, *42*). The energetics of proton binding on free water and ligand water were compared by DFT calculations to identify which one is the more energetically favorable binding site. We chose the smallest unit cell with the lowest energy as the starting compound. The VOx framework is omitted, and only water molecules are displayed for better visualization. We first modeled the protonated NZVO with a ligand hydronium, where the inserted H^+ is highlighted in blue (fig. S23). After relaxation, the inserted H^+ migrates to a free water site, suggesting the lower energy of the free water site for H^+ binding than ligand water site. We also computed a protonated NZVO with a free hydronium, which still remains the free hydronium configuration after relaxation (fig. S24), further validating that the free water is energetically preferable for H^+ binding. The O atom of the ligand water is strongly bound to the transition metal cations, impeding the formation of the ligand hydronium. A similar phenomenon that a hydronium cation prevents other cations from coordinating with its O atom also supports the above result (*21*, *41*). DFT calculations confirm that the terminal O coordinated with V is also the energetically favorable H^+ binding site. The protonated NZVO with H^+ binding with terminal oxygen still retains the configuration besides some subtle orientation adjustments after relaxation (fig. S25). The remaining edge-sharing O coordinated with V atoms is not favorable for H^+ binding because all O 2p orbitals (2px, 2py, and 2pz) bond to the V_{3d}-O_{2p} orbitals.

To further explore the proton transport mechanism in the NZVO electrode, we calculated the energy barrier of three representative proton transport pathways by DFT method. The first pathway is along a water chain, from a free water to the neighboring ligand water then to another free water (Fig. 4, A to D). The energy variation during proton transport is displayed in Fig. 4D. All the configurations of the protonated NZVO structure at different transition stage are provided in fig. S26. At stage 1, the proton binds with the initial free water, and their energies are similar. From stage 2 to stage 3, the proton hops from a free water to a neighboring ligand water and the H-bonded water molecules reorientate, corresponding to an energy increase of ~0.12 eV. After the stage 4, the total energy begins to decrease, due to the proton hopping to a next free water so as to find a more stable configuration. The second pathway is among free water molecules (Fig. 4, E to H, and fig. S27). At stage 1, the proton stays with the first free water, corresponding to the lowest energy level. From stage 2 to stage 5, the proton hops from the first free water to the next free water along the H-bond chain accompanied by the reorientation of the H-bonded water molecules, leading to an energy increase of ~0.091 eV. Then, the proton hops to next free water to reach a more steady state, resulting in the decrease of total energy. The third pathway is from the terminal O coordinated with V to free water (Fig. 4, I to L, and fig. S28). At stage 1, the proton stays with the terminal O, and the energy level is the lowest. From stage 2 to stage 4, the proton hops from the terminal O to a neighboring free water along the HB and the H-bonded water molecules reorientate, accompanied with the increase of the total energy of ~0.084 eV. The energy decreases after stage 4 result from the proton hopping from the neighboring free water to a next free water to reach a more stable configuration.

The first proton transport pathway has an activation energy of about 0.03 eV more than the other two, arising from the ligand water molecule of which the rotation is somewhat confined by the lattice. The confinement effect of ligand water is further manifested with calculations. The activation energy of proton transport in a hypothetical NZVO cathode with only ligand water molecules where proton transfer unidirectionally is calculated to be ~0.26 eV (fig. S29), much higher than that in the practical NZVO with both free and ligand water. The result also demonstrates the importance of free water in facilitating proton transport, by providing the freedom to adjust to needed orientations and configurations as suggested by calculations (*24*, *25*). Previous experimental and theoretical studies have suggested that the apparent activation energy of proton transfer in bulk water is 2.4 to 2.7 kcal/mol (0.10 to 0.12 eV) (*43*, *44*). The calculated proton transport energy barriers (0.08 to 0.12 eV) in NZVO are very close to this range, suggesting bulk-like fast transfer kinetics.

Electrochemical performance of Zn/NZVO batteries

Benefiting from the ultrafast charge transfer kinetics endowed by the unique proton special pair dance mechanism, the Zn/NZVO battery exhibits an outstanding rate capability, delivering capacities of 436, 410, 397, 374, 357, 325, 268, 205, 155, 118, and 92 mA h g^{-1} at rates of 0.5, 2.5, 5, 12.5, 25, 50, 125, 250, 500, 750, and 1000 C, respectively (Fig. 5A). Figure S30 displays the corresponding charge/discharge profiles at various rates. Moreover, the discharge capacity recovers to 457 mAh g^{-1} when the rate abruptly decreases from 1000 C to 0.5 C, suggesting the robust structure of NZVO electrode. At an extremely high rate of 1000 C, the Zn/NZVO battery can be fully charged/discharged in less than 2 s. Such a high rate capability is comparable with that of electrodes in capacitors and surpasses those of most Faradaic electrodes. The high-rate performance is further evidenced in the Ragone plot (Fig. 5B). The Zn/NZVO battery achieves an energy density of 315.3 Wh kg^{-1} at a power density of 146.9 W kg^{-1} and maintains 103.6 Wh kg^{-1} at a very high power density of 162 kW kg^{-1} (based on the mass of NZVO), superior to previously reported aqueous proton and Zn ion cells/capacitors (tables S4 and S5) (*12*, *20*, *37*, *45*–*52*).

To gain insight into the high-rate capability of the NZVO electrode, the electrochemical kinetics were studied by CV measurements at various scan rates (Fig. 5C and fig. S31). The currents at various scanning rates are all measured over the 100% of step duration to keep consistent, thereby leading to comparable results (note S3). The relationship between the peak current (i) and the sweep rate (v) complies with the following power-law formula: $i = av^b$, where a and b refer to adjustable parameters. In addition, the b value could evaluate the electrochemical behavior of the electrode. Specifically, the b value of 0.5 indicates that the kinetics were controlled by semi-infinite linear diffusion, whereas a value of 1 represents capacitive-type behavior (*53*). As shown in Fig.5C and fig. S30A, when scan rates are in the range of <20 mV s^{-1}, the CV curves have two separated reduction peaks and two distinct oxidation peaks, revealing multistep (de)intercalation processes. When the scan rate increases higher than 20 mV s^{-1}, the two anodic or cathodic peaks merge into one (fig. S31B). For scan rates from 0.2 to 20 mV s^{-1}, the b values of the four peaks are close to 1 and presented as 0.91, 0.99, 0.96, and 0.93, indicating that the charge storage is mainly surface-controlled (Fig. 5D). Beyond that, the b values for the anodic and cathodic peaks are 0.59 and 0.68, revealing

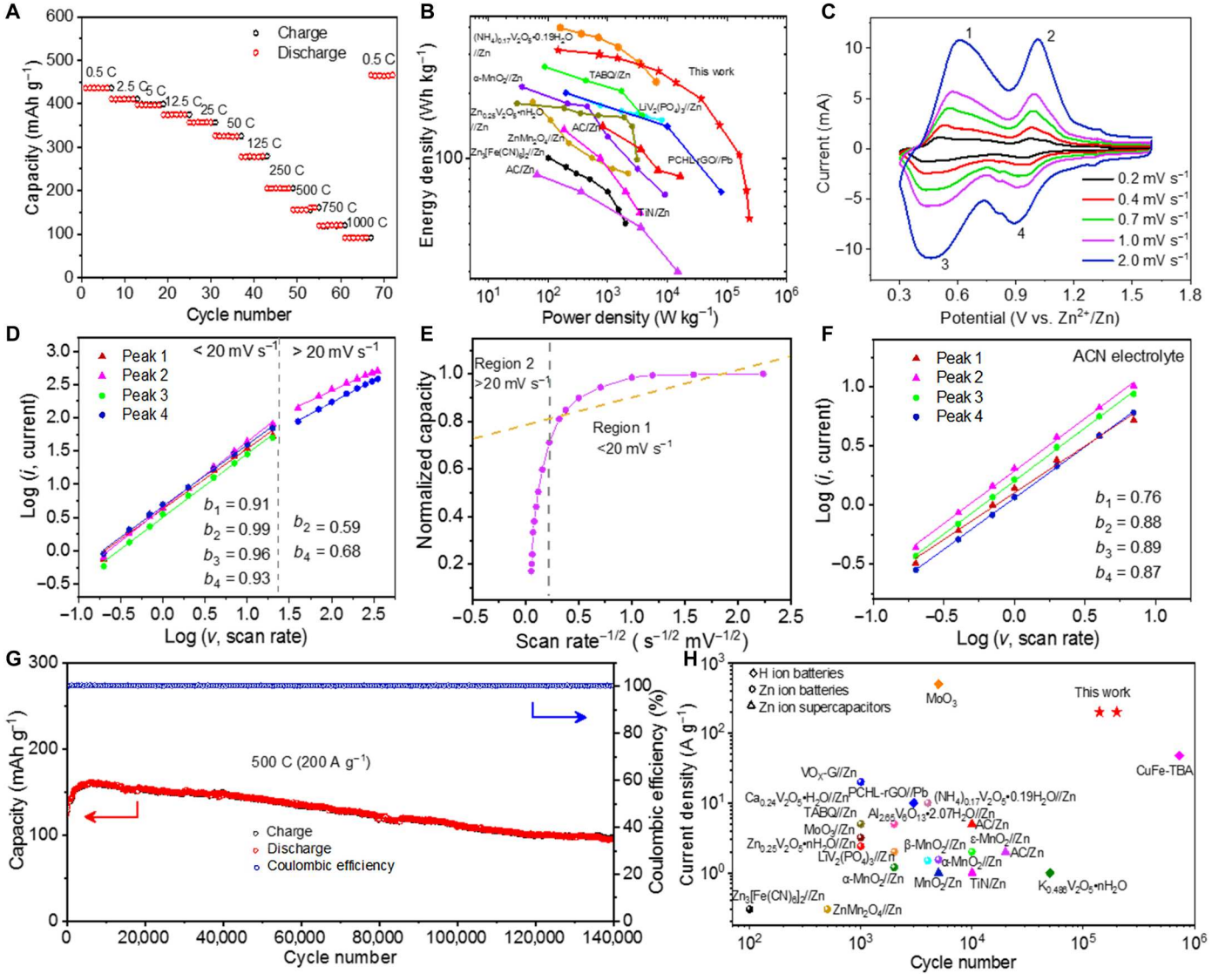

Fig. 5. Electrochemical performances of Zn/NZVO batteries in 3 M $Zn(CF_3SO_3)_2$ aqueous electrolyte. (**A**) Rate performance between 0.5 and 1000 C (1 C = 400 mA g^{-1}). (**B**) Ragone plot of Zn/NZVO battery and previously reported representative aqueous proton and Zn ion cells/capacitors (based on mass of cathode active materials). (**C**) CV curves of Zn/NZVO batteries at scan rates from 0.2 to 2.0 mV s^{-1}. (**D**) Corresponding plots of log(*i*) versus log(*v*) at cathodic and anodic peaks. (**E**) Normalized capacity versus $v^{-1/2}$ curves at scan rates of 0.2 to 350 mV s^{-1}. (**F**) Corresponding plots of log(*i*) versus log(*v*) at cathodic and anodic peaks in 3 M $Zn(CF_3SO_3)_2$ ACN electrolyte. (**G**) Cycling performance of Zn/NZVO battery at a rate of 500 C for 0.14 million cycles. (**H**) Comparison of current density and cycle life of the Zn/NZVO battery with reported aqueous proton and Zn ion cells/capacitors.

that a semi-infinite diffusion dominates the kinetics. Moreover, the correlation between capacity and sweep rate is also investigated to reflect the rate-limiting step during charge/discharge. There are two distinct regions in the plot of normalized capacity versus $v^{-1/2}$ in the rate range of 0.1 to 350 mV s^{-1} (Fig. 5E). In region 2 (scanning rates > 20 mV s^{-1}), the capacity is almost dependent with $v^{-1/2}$, suggesting that the solid-state H^+/Zn^{2+} diffusion is the rate-limiting step. In contrast, the capacity contribution is hardly correlated with the sweep rate in region 1 (scanning rates < 20 mV s^{-1}), suggesting a pseudocapacitive manner. The rate-limiting step transformation from surface-controlled to diffusion-controlled at the watershed sweep rate of 20 mV s^{-1} may result from an increase in ohmic impedance such as electrode-electrolyte interphase resistance, or diffusion constraints (*53*). The current response (*i*) at a fixed potential (*V*) can be divided into the capacitive current (k_1v) and diffusion-controlled current ($k_2v^{1/2}$) according to the following equation: $i = k_1v + k_2v^{1/2}$. (*54*) By fitting the linear relationship between $i/(v^{1/2})$ and $v^{1/2}$, the slope k_1 and intercept k_2 can be determined (fig. S32A). The capacitive current contribution to the total capacity at 0.2 mV s^{-1} is 84.5% and increases to 94.3% at 2 mV s^{-1} (fig. S32, B and C), indicating that the pseudocapacitive contribution is dominant from 0.2 to 2 mV s^{-1}. In contrast, the *b* values of the redox peaks in 3 M $Zn(CF_3SO_3)_2$/ACN electrolyte are 0.76, 0.88, 0.89, and 0.87 with scan rates from 0.2 to 7 mV s^{-1} (Fig. 5F and fig. S33), which are smaller than those aqueous counterparts, revealing sluggish electrochemical kinetics without H^+ (de)insertion. Hence,

the unique proton conduction is essential for the ultrafast electrochemical kinetics of NZVO. The Zn/NZVO battery delivers excellent cycle stability at various rates (Fig. 5G and fig. S34). Impressively, a long-term stability of over 0.14 million cycles at 500 C was achieved, with a capacity retention of 78% and coulombic efficiency (CE) approaching 99% (Fig. 5G), which exceeds most previously reported aqueous proton and Zn ion cells/capacitors (Fig. 5H and tables S4 and S5) (*10*, *12*, *15*–*20*, *37*, *45*–*52*, *55*–*60*). The average CE of Zn/NZVO cells cycled at various rates approaches 100% and reaches 100.32% at 200 A g^{-1} based on 100% H^+ insertion (fig. S35A). The CE increases with the charge/discharge rate, which follows the trend of H^+ insertion contribution to the total capacity. In addition, the CE remains almost constant during stable cycles and decreases at last (fig. S35, B to E). It is worth noting that electrolyte oxidation will notably reduce the cycle performance of a real cell with lean electrolyte. In addition, the zinc is being oxidized in the anode, but protons are contributing to the capacity of NZVO, which suggests that there is a net uptake of Zn ions in the electrolyte. Therefore, long cycles require excess electrolyte. With limited electrolyte, this can cause precipitation or conductivity issues that reduce the cycle life (fig. S36). A low N:P (negative-to-positive electrode capacity) ratio is a key parameter to achieve high energy density of a full battery. The full Zn/NZVO cells with N:P ratio of 9.3:1 (fig. S37, A and B) exhibited a stable discharge capacity of ~106 mAh g^{-1} and high CE for 50,000 cycles at 100 A g^{-1} (fig. S38A). When the N:P ratio reduces to 5.2:1 (fig. S37, C and D), the full cells also demonstrated high capacity retention of 79% over 30,000 cycles (fig. S38B), outperforming other proton full cells (fig. S39 and table S6) (*10*, *51*, *59*–*62*).

Structural evolution during proton (de)intercalation

To better understand the exceptional cycling stability of NZVO electrode, ex situ XRD was carried out to reveal the structural evolution of NZVO electrode with the proton (de)intercalation. As displayed in Fig. 6A and fig. S40, NZVO maintains its typical layered structure during the proton insertion/extraction processes. Moreover, the peak position of (001) reflection remains almost unchanged with the proton (de)intercalation. The differential charge density analysis shows that the insertion of H^+ alters charge distribution in NZVO (fig. S41). There is an accumulation of charge localized mostly on the terminal oxygen atom coordinated with the inserted H^+, whereas the electronic charge around H^+ sites decreases, resulting in a higher chemical shift. The ^1H nuclear magnetic resonance peak at 4.03 ppm becomes broader and shifts to a higher chemical shift after discharge (Fig. 6B), confirming the H^+ insertion. The subtle lattice variation after 10 protons inserts into each NZVO unit cell indicates the proton inserts into the lattice in the form of H^+ at the high rate of 200 A g^{-1}. If 10 protons insert in the form of H_3O^+, the lattice would expand obviously after discharge, which is inconsistent with the XRD result. At low discharge rates (<200 A g^{-1}), partial hydrated Zn^{2+} ions insert into the cathode lattice, and protons might bind with solvated water of Zn^{2+} ions and insert into the cathode lattice in the form of H_3O^+, which warrants further investigation. The crystal structure after the proton insertion was simulated to specify the corresponding changes (Fig. 6C). After insertion of 10 protons in per unit cell, which produces a specific capacity of 147 mAh g^{-1}, the interlayer space of (001) plane enlarges from 12.75 to 12.85 Å, and the lattice expansion can be calculated to be ~0.78%, well in accordance with the slight left shift of (001) peak in XRD results (Fig. 6A). The corresponding volume expansion is calculated to be very little, only ~2.43%. The zero strain-like behavior with minimal change in both host structure and interlayer space contributes to the cycling stability. The special pair dance mechanism occurs at a time scale of tens of femtoseconds (10^{-15} s), and the orientational dynamic signal of lattice water in ultrafast infrared spectroscopy measurement is submerged in that of carrier due to the fact that NZVO is a kind of vanadium oxide semiconductor (fig. S42 and note S4). Thus, we were not able to observe the real-time proton transfer dynamics with technologies available to us. Further study is needed in the future.

It is well known that the electrolyte anion is critical for the cycling stability of aqueous zinc batteries with Zn^{2+} as charge shuttle (*14*, *58*). For instance, the replacement of $CF_3SO_3^-$ with SO_4^{2-} can result in much faster capacity decay in certain battery systems due to lower ionic conductivity (*14*, *58*). To our delight, with proton as the charge carrier, the cycling stability of the Zn/NZVO battery is hardly affected by anion. Similar to those using 3 M $Zn(CF_3SO_3)_2$ aqueous electrolyte (Fig. 5G), the Zn/NZVO battery exhibits a remarkable cycling stability in 3 M $ZnSO_4$ aqueous electrolyte. Seventy-six percent of its initial capacity is retained with coulombic efficiency (CE) approaching 99% after 0.2 million cycles at 500 C (Fig. 6D). The huge difference of cycle life between H^+ and Zn^{2+} as charge carrier is likely because the diffusive nature of hydrated proton makes it not as easy as those metal cations to form ion clusters in concentrated aqueous solutions (*63*).

DISCUSSION

In summary, an aqueous battery with rate and cycle life orders of magnitude improved from previous Faradaic batteries is successfully developed. Comprehensive experimental and theoretical results suggest that a 3D dense hydrogen-bonding network provides indispensable solvation environment for protons to rapidly switch between the Zundel and Eigen configurations and diffuse in 3D directions with low energy barriers and little volume change. The unique special pair dance mechanism endows proton with much faster transfer kinetics than the sluggish kinetics of metal cation Zn^{2+}. Moreover, the little volume change resulting from proton transfer can effectively avoid structural stress and failure caused by electrochemical cycling. Both factors respectively contribute to the supercapacitor-like high power density and long cycling stability. Zn^{2+} also contributes to charge transport, but its contribution is negligible at high rates. The unique proton transport mechanism also leads to a very notable feature that the performance of the full battery is nearly independent of the choice of anion in the electrolyte, which is important for practical applications. This work provides insight into developing high-power and long-life electrochemical energy storage devices with nonmetal ion transfer through special pair dance topochemistry dictated by HB. The occurrence of special pair dance topochemistry relies on a dense and interconnected HB network. Hence, the design of electrode materials with a large interlayer distance (>1 nm) and plenty of medium should be considered to allow the special pair dance topochemistry, thereby achieving high power density.

To promote the practical application of Zn/NZVO batteries, improving energy density is also a key point. On one hand, introducing electron-withdrawing groups, such as PO_4^{3-} and F^-, into the host structure can increase the average operation voltage, thus

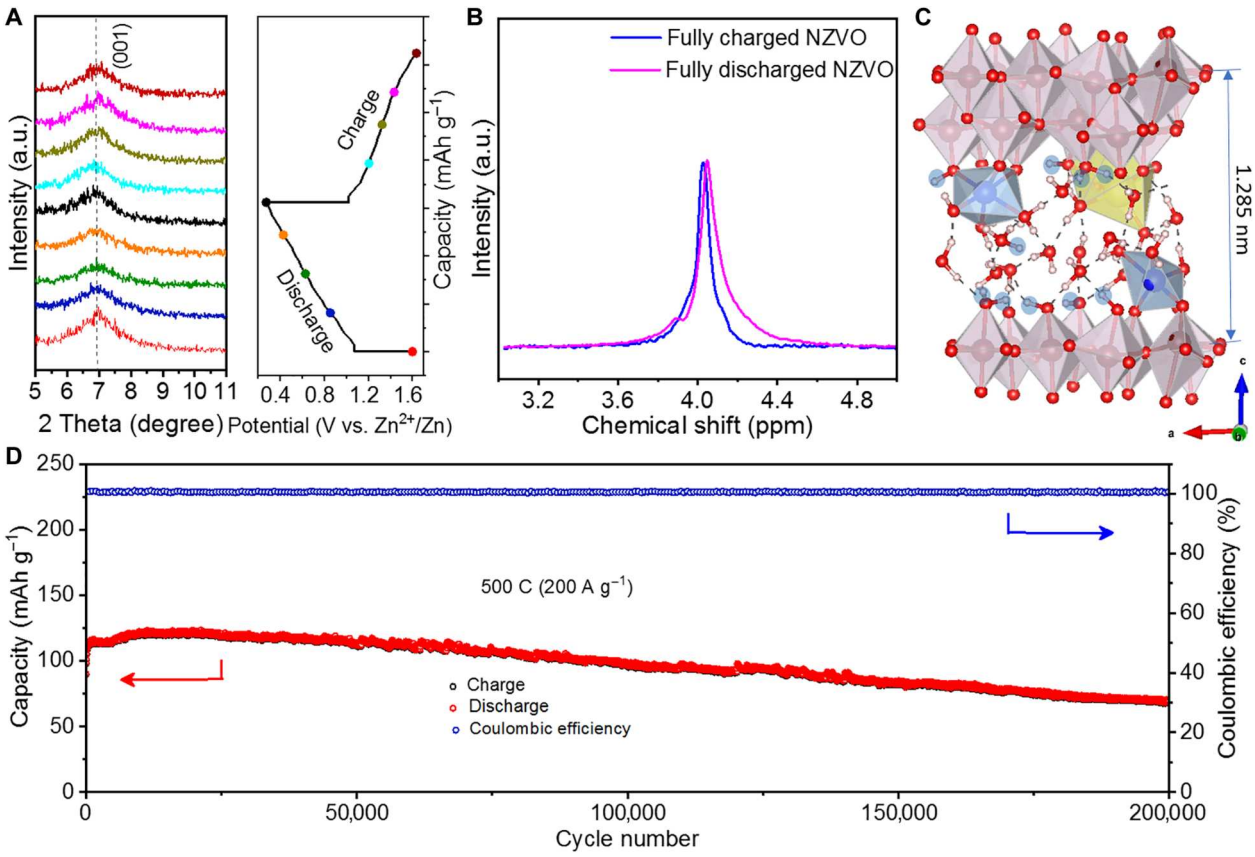

Fig. 6. Structural evolution during proton (de)insertion. (**A**) Enlarged view of the (001) peak from the XRD patterns of NZVO electrode at 500 C (200 A g^{-1}) as a function of discharge and charge voltage. (**B**) Solid-state ^{1}H nuclear magnetic resonance (NMR) spectra of the fully charged/discharged NZVO at 500 C. (**C**) Calculated structure of fully discharged NZVO. (**D**) Cycling performance of Zn/NZVO battery in 3 M $ZnSO_4$ aqueous electrolyte at a rate of 500 C for 0.2 million cycles.

leading to higher energy density. On the other hand, designing hierarchical porous structure can not only improve compaction density but also guarantee good kinetics by facilitating rapid ion transport and mitigating diffusion limitations throughout the entire electrode, which needs further investigation in future.

MATERIALS AND METHODS

Preparation of 3D NVO networks

The 3D-NVO was prepared by a facile and scalable electrodeposition technique. The electrochemical deposition was carried out at room temperature in a three-electrode cell with graphite substrate as the working electrode and a platinum sheet as both counter and reference electrodes in the 0.2 M $VOSO_4$ + 0.2 M $NaCH_3COO$ aqueous solution. The three-electrode cell was galvanostatically charged at 2 mA cm^{-2} for 20 hours using a LAND-CT2001A battery test system. The electrodeposition reaction at the working electrode is as below: $2VO^{2+} + 0.27Na^{+} - 1.73e^{-} + 4.53H_2O \rightarrow Na_{0.27}V_2O_5{\cdot}1.53H_2O + 6H^{+}$. Moreover, the electrolysis of H_2O may also occur at the working electrode: $2H_2O \rightarrow O_2 + 4e^{-} + 4H^{+}$. There are only oxidation reactions on graphite substrate electrode during NVO electrodeposition. Thus, cations including Na^{+} and H^{+} in electrolyte cannot be inserted into graphite substrate and do not participate in the electrochemical reaction at graphite electrode. After deposition, the as-deposited product was collected from the electrode, rinsed with deionized water and ethanol, and dried in vacuum at 60°C for 24 hours.

Electrochemical measurements

Electrochemical performance was assessed using CR2032 coin-type cells assembled in air. Active materials were mixed with Ketjen black (ECP600JD), conducting Super P and a water-based composite binder (CMC), and SBR in a 70:18:6:4:2 weight ratio. The slurry was then pasted onto stainless steel (SUS 304) foil and vacuum-dried at 60°C for 12 hours. The mass loading of the active material is ~1 and ~1.6 mg cm^{-2} in half cells and full cells, respectively. Aqueous solution [3 M $Zn(CF_3SO_3)_2$/3 M $ZnSO_4$] and glass fiber membrane were used as electrolyte and separator, respectively. In each coil cell, ~100 μl of electrolyte was added by pipette to make sure the electrodes and the separator were wetted. For half-cell measurements, commercial 100-μm-thick Zn foil was used as the anode. For full cell measurements, electrodeposited Zn on graphite paper served as anodes. The Zn anodes are prepared by electrodeposition in 1 M $ZnSO_4$ aqueous electrolyte at 5 mA cm^{-2} to precisely control the amount of Zn (6.5 and 3.6 mAh cm^{-2}) and therefore the N:P ratio (9.3:1 and 5.2:1). CV measurements at various scan rates and EIS were conducted using a CHI760C electrochemical workstation.

Characterizations

The crystal structure of the electrode was characterized by x-ray diffraction (Rigaku Dmax/2400 diffractometer with Cu Kα radiation, 40 kV, 100 mA). The morphology was analyzed by a field emission scanning electron microscope (S4800, Hitachi) and a transmission electron microscope (JEM-2100, JEOL) equipped with EDS for elemental analysis. The elemental oxidation states were examined by XPS (Axis Ultra, Kratos Analytical Ltd.). All XPS spectra were calibrated with respect to the C1s peak binding energy of 284.8 eV. The water content was investigated using TGA (SDT Q600) with a temperature ramp of 10°C min^{-1} in N_2 atmosphere. The specific surface areas and pore structures were obtained by N_2 adsorption-desorption measurement (Micrometrics ASAP 2020). The molar ratio of Na to V was measured by using ICP–atomic emission spectroscopy (ICP-AES; Leeman, Prodigy 7).

Proton conductivity tests

The NVO powder was first compressed into a pellet with a diameter of 16 mm and a thickness of 0.16 mm. Then, the pellet was assembled into a coin cell, in which a wet cotton ball immersed with 0.005 M H_2SO_4 aqueous electrolyte was placed to maintain the 100% humidity during tests. During the EIS tests, the oscillation amplitude was set as 20 mV and the frequencies range from 1 MHz to 0.1 Hz. The proton conductivity was determined by the following equation (*39*, *64*)

$$\sigma = L/RS \quad (1)$$

where σ, L, S, and R_b represent the proton conductivity (S cm^{-1}), thickness of pellet (cm), contact area (cm^2), and bulk resistance (ohm), respectively. We conducted EIS tests at different temperatures and calculated the corresponding proton conductivities. The activation energies (E_a) can be calculated according to the following equation (*39*, *65*)

$$\ln(\sigma T) = \ln A\text{-}E_a/k_B T \quad (2)$$

where T, A, k_B, and E_a are the temperature, preexponential factor, Boltzmann constant, and activation energy for proton conduction, respectively.

First-principles calculations

The Vienna Ab initio Simulation Package (VASP) (*66*, *67*) was implemented under the projector wave pseudopotentials (*68*) with the generalized gradient approximation of the Perdew-Burke-Ernzerh (*69*) of exchange-correlation function. An energy cutoff of 400 eV with a Monkhorst-Pack (*70*) reciprocal space grid of a 1 × 1 × 1 k-point scheme was used for the unit cell structure, which has a specific stoichiometry of Na/Zn/V/H_2O = 1/2/16/40/20. All geometrical structures were fully optimized to its ground state. The convergence criteria for the total energy and the maximum force on each atom are less than 1×10^{-5} eV and 0.05 eV/Å, respectively. In addition, the climbing image nudged elastic band (CI-NEB) method was used to determine the minimum energy diffusion pathways of ions and the corresponding energy barriers.

FPMD simulations

Since ~10 protons can be stored in each wet NZVO unit cell (1Na2Zn16V40O·20H_2O) at 200 A g^{-1}, three protons were randomly inserted into the (001) interlayer of each NZVO unit cell to simulate an early stage of the discharge process. After the configuration optimization, FPMD simulations were performed in canonical ensemble (NVT) with Nose thermostat at 300 K over a period of 16 ps with a time step of 1 fs (*71*, *72*). To reach equilibrium, the system was heated to 300 K by a thermostat over a few picoseconds. Once equilibration was achieved, we removed the thermostat and molecular dynamic trajectories were collected. From the time-dependent trajectory of O_0 (oxygen atom of the hydronium ion), we can obtain its time-dependent MSD

$$\langle r^2(t)\rangle = \frac{1}{N \times n_t}\sum_{t_0=0}^{n_t}\sum_{i=0}^{N}[R_i(t_0+\Delta t) - R_i(t_0)]^2$$

where N is the total number of atoms, n_t is the total number of t, and $R_i(t_0)$ and $R_i(t_0 + t)$ represent the positions of the ith O atom at time t_0 and $t_0 + t$, respectively. To evaluate the contribution from different directions, we also decomposed MSD to x, y, and z direction by projecting the position to the relative direction. The diffusion coefficients were evaluated by using the Einstein relation, $D = \frac{1}{6}\frac{\partial(\mathrm{MSD})}{\partial t}$. Proton diffusion in bulk water was simulated in a cubic unit cell of 12.36 Å in length containing 63 water molecules and one excess proton.

Supplementary Materials

This PDF file includes:

Figs. S1 to S42
Tables S1 to S6
Notes S1 to S4
Legend for movie S1

Other Supplementary Material for this manuscript includes the following:

Movie S1

REFERENCES AND NOTES

1. P. Simon, Y. Gogotsi, B. Dunn, Where do batteries end and supercapacitors begin? *Science* **343**, 1210–1211 (2014).
2. B. Kang, G. Ceder, Battery materials for ultrafast charging and discharging. *Nature* **458**, 190–193 (2009).
3. M. Armand, J. M. Tarascon, Building better batteries. *Nature* **451**, 652–657 (2008).
4. Z. Yang, J. Zhang, M. C. W. Kintner-Meyer, X. Lu, D. Choi, J. P. Lemmon, J. Liu, Electrochemical energy storage for green grid. *Chem. Rev.* **111**, 3577–3613 (2011).
5. X. W. Lou, D. Deng, J. Y. Lee, J. Feng, L. A. Archer, Self-supported formation of needlelike Co_3O_4 nanotubes and their application as lithium-ion battery electrodes. *Adv. Mater.* **20**, 258–262 (2008).
6. B. L. Ellis, L. F. Nazar, Sodium and sodium-ion energy storage batteries. *Curr. Opin. Solid State Mater. Sci.* **16**, 168–177 (2012).
7. M. Mao, T. Gao, S. Hou, C. Wang, A critical review of cathodes for rechargeable mg batteries. *Chem. Soc. Rev.* **47**, 8804–8841 (2018).
8. C. Yang, J. Chen, X. Ji, T. P. Pollard, X. Lu, C.-J. Sun, S. Hou, Q. Liu, C. Liu, T. Qing, Y. Wang, O. Borodin, Y. Ren, K. Xu, C. Wang, Aqueous li-ion battery enabled by halogen conversion–intercalation chemistry in graphite. *Nature* **569**, 245–250 (2019).
9. Z. Zhu, W. Wang, Y. Yin, Y. Meng, Z. Liu, T. Jiang, Q. Peng, J. Sun, W. Chen, An ultrafast and ultra-low-temperature hydrogen gas-proton battery. *J. Am. Chem. Soc.* **143**, 20302–20308 (2021).
10. X. Wu, J. J. Hong, W. Shin, L. Ma, T. Liu, X. Bi, Y. Yuan, Y. Qi, T. W. Surta, W. Huang, J. Neuefeind, T. Wu, P. A. Greaney, J. Lu, X. Ji, Diffusion-free grotthuss topochemistry for high-rate and long-life proton batteries. *Nat. Energy* **4**, 123–130 (2019).
11. Z. Guo, J. Huang, X. Dong, Y. Xia, L. Yan, Z. Wang, Y. Wang, An organic/inorganic electrode-based hydronium-ion battery. *Nat. Commun.* **11**, 959 (2020).
12. Z. Lin, H. Y. Shi, L. Lin, X. Yang, W. Wu, X. Sun, A high capacity small molecule quinone cathode for rechargeable aqueous zinc-organic batteries. *Nat. Commun.* **12**, 4424 (2021).

13. Y. Xu, X. Wu, X. Ji, The renaissance of proton batteries. *Small Structures* **2**, 2000113 (2021).
14. L. Wang, K.-W. Huang, J. Chen, J. Zheng, Ultralong cycle stability of aqueous zinc-ion batteries with zinc vanadium oxide cathodes. *Sci. Adv.* **5**, eaax4279 (2019).
15. H. Huang, X. Xia, J. Yun, C. Huang, D. Li, B. Chen, Z. Yang, W. Zhang, Interfacial engineering of hydrated vanadate to promote the fast and highly reversible H^+/Zn^{2+} co-insertion processes for high-performance aqueous rechargeable batteries. *Energy Storage Mater.* **52**, 473–484 (2022).
16. T. Lv, G. Zhu, S. Dong, Q. Kong, Y. Peng, S. Jiang, G. Zhang, Z. Yang, S. Yang, X. Dong, H. Pang, Y. Zhang, Co-intercalation of dual charge carriers in metal-ion-confining layered vanadium oxide nanobelts for aqueous zinc-ion batteries. *Angew. Chem. Int. Ed.* **62**, e202216089 (2022).
17. Q. Zhao, A. Song, W. Zhao, R. Qin, S. Ding, X. Chen, Y. Song, L. Yang, H. Lin, S. Li, F. Pan, Boosting the energy density of aqueous batteries via facile grotthuss proton transport. *Angew. Chem. Int. Ed.* **60**, 4169–4174 (2020).
18. H. Zhang, W. Wu, Q. Liu, F. Yang, X. Shi, X. Liu, M. Yu, X. Lu, Interlayer engineering of α-MoO_3 modulates selective hydronium intercalation in neutral aqueous electrolyte. *Angew. Chem. Int. Ed.* **60**, 896–903 (2020).
19. W. Sun, F. Wang, S. Hou, C. Yang, X. Fan, Z. Ma, T. Gao, F. Han, R. Hu, M. Zhu, C. Wang, Zn/MnO_2 battery chemistry with H^+ and Zn^{2+} coinsertion. *J. Am. Chem. Soc.* **139**, 9775–9778 (2017).
20. M. Li, Y. Zhang, J. Hu, X. Wang, J. Zhu, C. Niu, C. Han, L. Mai, Universal multifunctional hydrogen bond network construction strategy for enhanced aqueous Zn^{2+}/proton hybrid batteries. *Nano Energy* **100**, 107539 (2022).
21. N. Agmon, The grotthuss mechanism. *Chem. Phys. Lett.* **244**, 456–462 (1995).
22. W. M. Latimer, W. H. Rodebush, Polarity and ionization from the standpoint of the lewis theory of valence. *J. Am. Chem. Soc.* **42**, 1419–1433 (1920).
23. M. L. Huggins, Hydrogen bridges in ice and liquid water. *J. Phys. Chem.* **40**, 723–731 (1936).
24. P. B. Calio, C. Li, G. A. Voth, Resolving the structural debate for the hydrated excess proton in water. *J. Am. Chem. Soc.* **143**, 18672–18683 (2021).
25. O. Markovitch, H. Chen, S. Izvekov, F. Paesani, G. A. Voth, N. Agmon, Special pair dance and partner selection: Elementary steps in proton transport in liquid water. *J. Phys. Chem. B* **112**, 9456–9466 (2008).
26. M. Tuckerman, K. Laasonen, M. Sprik, M. Parrinello, Ab initio molecular dynamics simulation of the solvation and transport of H_3O^+ and OH^- ions in water. *J. Phys. Chem.* **99**, 5749–5752 (1995).
27. J. K. Gregory, D. C. Clary, K. Liu, M. G. Brown, R. J. Saykally, The water dipole moment in water clusters. *Science* **275**, 814–817 (1997).
28. M. C. Pitman, A. C. van Duin, Dynamics of confined reactive water in smectite clay–zeolite composites. *J. Am. Chem. Soc.* **134**, 3042–3053 (2012).
29. E. E. Fenn, D. B. Wong, M. D. Fayer, Water dynamics at neutral and ionic interfaces. *Proc. Natl. Acad. Sci. U.S.A.* **106**, 15243–15248 (2009).
30. Y. Sun, C. Zhan, P. R. C. Kent, M. Naguib, Y. Gogotsi, D. E. Jiang, Proton redox and transport in mxene-confined water. *ACS Appl. Mater. Interfaces* **12**, 763–770 (2020).
31. S. Roy, D. Skoff, D. V. Perroni, J. Mondal, A. Yethiraj, M. K. Mahanthappa, M. T. Zanni, J. L. Skinner, Water dynamics in gyroid phases of self-assembled gemini surfactants. *J. Am. Chem. Soc.* **138**, 2472–2475 (2016).
32. D. Laage, J. T. Hynes, A molecular jump mechanism of water reorientation. *Science* **311**, 832–835 (2006).
33. P. Hu, T. Zhu, X. Wang, X. Wei, M. Yan, J. Li, W. Luo, W. Yang, W. Zhang, L. Zhou, Z. Zhou, L. Mai, Highly durable $Na_2V_6O_{16}$ •1.63H_2O nanowire cathode for aqueous zinc-ion battery. *Nano Lett.* **18**, 1758–1763 (2018).
34. N. Ogihara, Y. Itou, T. Sasaki, Y. Takeuchi, Impedance spectroscopy characterization of porous electrodes under different electrode thickness using a symmetric cell for high-performance lithium-ion batteries. *J. Phys. Chem. C* **119**, 4612–4619 (2015).
35. N. Ogihara, S. Kawauchi, C. Okuda, Y. Itou, Y. Takeuchi, Y. Ukyo, Theoretical and experimental analysis of porous electrodes for lithium-ion batteries by electrochemical impedance spectroscopy using a symmetric cell. *J. Electrochem. Soc.* **159**, A1034–A1039 (2012).
36. H. Sun, L. Mei, J. Liang, Z. Zhao, C. Lee, H. Fei, M. Ding, J. Lau, M. Li, C. Wang, X. Xu, G. Hao, B. Papandrea, I. Shakir, B. Dunn, Y. Huang, X. Duan, Three-dimensional holey-graphene/niobia composite architectures for ultrahigh-rate energy storage. *Science* **356**, 599–604 (2017).
37. D. Kundu, B. D. Adams, V. Duffort, S. H. Vajargah, L. F. Nazar, A high-capacity and long-life aqueous rechargeable zinc battery using a metal oxide intercalation cathode. *Nat. Energy* **1**, 16119 (2016).
38. C. T. Wolke, J. A. Fournier, L. C. Dzugan, M. R. Fagiani, T. T. Odbadrakh, H. Knorke, K. D. Jordan, A. B. McCoy, K. R. Asmis, M. A. Johnson, Spectroscopic snapshots of the proton-transfer mechanism in water. *Science* **354**, 1131–1135 (2016).
39. S.-i. Ohkoshi, K. Nakagawa, K. Tomono, K. Imoto, Y. Tsunobuchi, H. Tokoro, High proton conductivity in prussian blue analogues and the interference effect by magnetic ordering. *J. Am. Chem. Soc.* **132**, 6620–6621 (2010).
40. T. S. Light, S. Licht, A. C. Bevilacqua, K. R. Morash, The fundamental conductivity and resistivity of water. *Electrochem. Solid State Lett* **8**, E16–E19 (2005).
41. C. Knight, G. A. Voth, The curious case of the hydrated proton. *Acc. Chem. Res.* **45**, 101–109 (2012).
42. D. Marx, M. E. Tuckerman, J. Hutter, M. Parrinello, The nature of the hydrated excess proton in water. *Nature* **397**, 601–604 (1999).
43. W. B. Carpenter, N. H. C. Lewis, J. A. Fournier, A. Tokmakoff, Entropic barriers in the kinetics of aqueous proton transfer. *J. Chem. Phys.* **151**, 034501 (2019).
44. Z. Luz, S. Meiboom, The activation energies of proton transfer reactions in water. *J. Am. Chem. Soc.* **86**, 4768–4769 (1964).
45. H. Pan, Y. Shao, P. Yan, Y. Cheng, K. S. Han, Z. Nie, C. Wang, J. Yang, X. Li, P. Bhattacharya, K. T. Mueller, J. Liu, Reversible aqueous zinc/manganese oxide energy storage from conversion reactions. *Nat. Energy* **1**, 16039 (2016).
46. N. Zhang, F. Cheng, Y. Liu, Q. Zhao, K. Lei, C. Chen, X. Liu, J. Chen, Cation-deficient spinel $ZnMn_2O_4$ cathode in $Zn(CF_3SO_3)_2$ electrolyte for rechargeable aqueous zn-ion battery. *J. Am. Chem. Soc.* **138**, 12894–12901 (2016).
47. F. Wang, E. Hu, W. Sun, T. Gao, X. Ji, X. Fan, F. Han, X.-Q. Yang, K. Xu, C. Wang, A rechargeable aqueous Zn^{2+}–battery with high power density and a long cycle-life. *Energy. Environ. Sci.* **11**, 3168–3175 (2018).
48. L. Zhang, L. Chen, X. Zhou, Z. Liu, Towards high-voltage aqueous metal-ion batteries beyond 1.5 V: The zinc/zinc hexacyanoferrate system. *Adv. Energy Mater.* **5**, 1400930 (2015).
49. P. Wang, X. Xie, Z. Xing, X. Chen, G. Fang, B. Lu, J. Zhou, S. Liang, H. J. Fan, Mechanistic insights of Mg^{2+}-electrolyte additive for high-energy and long-life zinc-ion hybrid capacitors. *Adv. Energy Mater.* **11**, 2101158 (2021).
50. Z. Huang, T. Wang, H. Song, X. Li, G. Liang, D. Wang, Q. Yang, Z. Chen, L. Ma, Z. Liu, B. Gao, J. Fan, C. Zhi, Effects of anion carriers on capacitance and self-discharge behaviors of zinc ion capacitors. *Angew. Chem. Int. Ed. Engl.* **60**, 1011–1021 (2021).
51. F. Yue, Z. Tie, S. Deng, S. Wang, M. Yang, Z. Niu, An ultralow temperature aqueous battery with proton chemistry. *Angew. Chem. Int. Ed. Engl.* **60**, 13882–13886 (2021).
52. L. Dong, X. Ma, Y. Li, L. Zhao, W. Liu, J. Cheng, C. Xu, B. Li, Q.-H. Yang, F. Kang, Extremely safe, high-rate and ultralong-life zinc-ion hybrid supercapacitors. *Energy Storage Mater.* **13**, 96–102 (2018).
53. V. Augustyn, J. Come, M. A. Lowe, J. W. Kim, P.-L. Taberna, S. H. Tolbert, H. D. Abruna, P. Simon, B. Dunn, High-rate electrochemical energy storage through Li^+ intercalation pseudocapacitance. *Nat. Mater.* **12**, 518–522 (2013).
54. T. Brezesinski, J. Wang, S. H. Tolbert, B. Dunn, Ordered mesoporous α-MoO_3 with iso-oriented nanocrystalline walls for thin-film pseudocapacitors. *Nat. Mater.* **9**, 146–151 (2010).
55. H. Wang, M. Wang, Y. Tang, A novel zinc-ion hybrid supercapacitor for long-life and low-cost energy storage applications. *Energy Storage Mater.* **13**, 1–7 (2018).
56. X. Ma, J. Cheng, L. Dong, W. Liu, J. Mou, L. Zhao, J. Wang, D. Ren, J. Wu, C. Xu, F. Kang, Multivalent ion storage towards high-performance aqueous zinc-ion hybrid supercapacitors. *Energy Storage Mater.* **20**, 335–342 (2019).
57. Y. Dai, X. Liao, R. Yu, J. Li, J. Li, S. Tan, P. He, Q. An, Q. Wei, L. Chen, X. Hong, K. Zhao, Y. Ren, J. Wu, Y. Zhao, L. Mai, Quicker and more Zn^{2+} storage predominantly from the interface. *Adv. Mater.* **33**, e2100359 (2021).
58. N. Zhang, F. Cheng, J. Liu, L. Wang, X. Long, X. Liu, F. Li, J. Chen, Rechargeable aqueous zinc-manganese dioxide batteries with high energy and power densities. *Nat. Commun.* **8**, 405 (2017).
59. W. Xu, K. Zhao, X. Liao, C. Sun, K. He, Y. Yuan, W. Ren, J. Li, T. Li, C. Yang, H. Cheng, Q. Sun, I. Manke, X. Lu, J. Lu, Proton storage in metallic $H_{1.75}MoO_3$ nanobelts through the grotthuss mechanism. *J. Am. Chem. Soc.* **144**, 17407–17415 (2022).
60. S. Dong, N. Lv, R. Ren, Y. Wu, P. Liu, G. Zhu, W. Wang, Y. Zhang, X. Dong, Ultralow-concentration electrolyte boosting $K_{0.486}V_2O_5$ for high-performance proton storage. *Sci. China Mater.* **65**, 3069–3076 (2022).
61. L. Yan, J. Huang, Z. Guo, X. Dong, Z. Wang, Y. Wang, Solid-state proton battery operated at ultralow temperature. *ACS Energy Lett.* **5**, 685–691 (2020).
62. Y. Liang, Y. Jing, S. Gheytani, K.-Y. Lee, P. Liu, A. Facchetti, Y. Yao, Universal quinone electrodes for long cycle life aqueous rechargeable batteries. *Nat. Mater.* **16**, 841–848 (2017).
63. H. Bian, X. Wen, J. Li, H. Chen, S. Han, X. Sun, J. Song, W. Zhuang, J. Zheng, Ion clustering in aqueous solutions probed with vibrational energy transfer. *Proc. Natl. Acad. Sci. U.S.A.* **108**, 4737–4742 (2011).
64. X. Y. Wu, M. M. Shao, C. H. Wu, J. F. Qian, Y. L. Cao, X. P. Ai, H. X. Yang, Low defect $FeFe(CN)_6$ framework as stable host material for high performance Li-ion batteries. *ACS Appl. Mater. Interfaces* **8**, 23706–23712 (2016).

65. K. Ono, M. Ishizaki, K. Kanaizuka, T. Togashi, T. Yamada, H. Kitagawa, M. Kurihara, Grain-boundary-free super-proton conduction of a solution-processed prussian-blue nanoparticle film. *Angew. Chem. Int. Ed.* **56**, 5531–5535 (2017).
66. G. Kresse, J. Furthmuller, Efficient iterative schemes for ab initio total-energy calculations using a plane-wave basis set. *Phys. Rev. B* **54**, 11169–11186 (1996).
67. G. Kresse, J. Hafner, Ab initio molecular-dynamics simulation of the liquid-metal–amorphous-semiconductor transition in germanium. *Phys. Rev. B* **49**, 14251–14269 (1994).
68. P. E. Blochl, Projector augmented-wave method. *Phys. Rev. B* **50**, 17953–17979 (1994).
69. J. P. Perdew, K. Burke, M. Ernzerhof, Generalized gradient approximation made simple. *Phys. Rev. Lett.* **77**, 3868–3865 (1996).
70. H. J. Monkhorst, J. D. Pack, Special points for brillouin-zone integrations. *Phys. Rev. B* **13**, 5188–5192 (1976).
71. S. Nose, A unified formulation of the constant temperature molecular-dynamics methods. *J. Chem. Phys.* **81**, 511–519 (1984).
72. D. M. Bylander, L. Kleinman, Energy fluctuations induced by the Nosé thermostat. *Phys. Rev. B* **46**, 13756–13761 (1992).

Acknowledgments: We thank S. Huang, C. Peng, and J. Ding from the College of Chemistry and Molecular Engineering in Peking University for the support of data analysis. We also thank J. Guan and X. Li from the College of Chemistry and Molecular Engineering in Peking University for the assistance in Ultrafast IR spectroscopy measurement. **Funding:** We acknowledge financial support from the National Science Foundation of China (NSFC-21927901, 92261206, 21627805, 12174012, and 21821004), MOST (2017YFA0204702 and special talent programs) of China, and China Postdoctoral Science Foundation (2022T150004). **Author contributions:** L.W. and J.Z. designed experiments. J.Y. carried out theoretical calculations. J.Z. supervised the project. L.W. and Y.H. performed experiments. J.Z., J.C., L.W., Z.Y. and J.Y. discussed experiments and results. L.W. and J.Z. prepared and revised the manuscript. **Competing interests:** The authors declare that they have no competing interests. **Data and materials availability:** All data needed to evaluate the conclusions in the paper are present in the paper and/or the Supplementary Materials.

Submitted 23 October 2022
Accepted 29 March 2023
Published 5 May 2023
10.1126/sciadv.adf4589

ScienceAdvances

Ultrahigh-rate and ultralong-life aqueous batteries enabled by special pair-dancing proton transfer

Lulu Wang, Jie Yan, Yuexian Hong, Zhihao Yu, Jitao Chen, and Junrong Zheng

Sci. Adv. **9** (18), eadf4589. DOI: 10.1126/sciadv.adf4589